

Advancing Bulk Metallic Glass Formation: Utilizing Rare-Earth Elements in Zr-Based Alloys



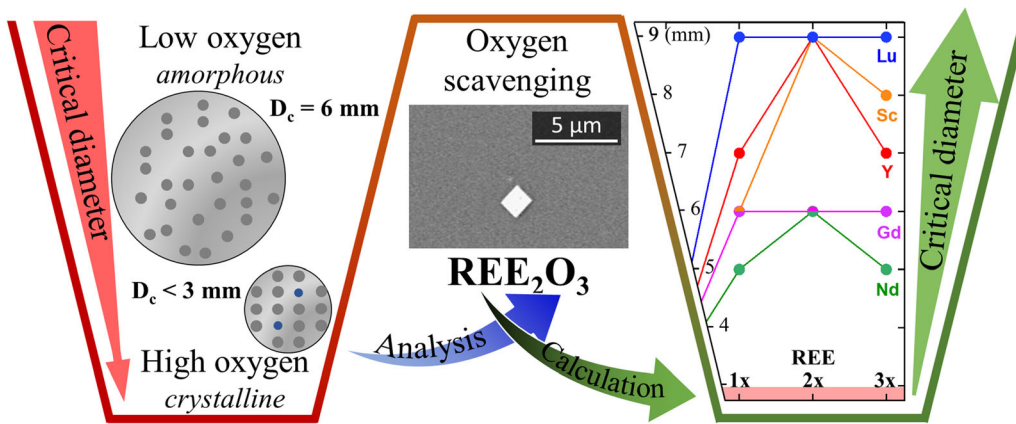
KRZYSZTOF PAJOR, ŁUKASZ GONDEK, DOROTA TYRAŁA, PIOTR BŁYSKUN, ŁUKASZ CIENIEK, and TOMASZ KOZIEŁ

Zr-based bulk metallic glasses (BMGs) are characterized by excellent glass-forming ability, combined with superior mechanical properties. However, oxygen impurities degrade both these aspects as oxides serve as heterogeneous nucleation sites during solidification. Rare-earth elements (REEs) are known to be good oxygen scavengers, binding oxygen to less harmful forms. The most stable rare-earth oxide (REO) is M_2O_3 , which occurs in three polymorphic forms, depending on the radius of metal cation: cubic, hexagonal, and monoclinic. Here, we show the effect of Sc, Y, Lu, Nd, and Gd additions in relation to the oxygen content on the glass-forming ability of the $Zr_{52.5}Cu_{17.9}Ni_{14.6}Al_{10}Ti_5$ alloy. Microscopic observations (SEM) supported by chemical analysis (EDS, WDS), structure identification (XRD), and thermal analysis (DTA) were carried out. The critical diameter for glass formation (D_c) in the high oxygen alloy doped with cubic oxide-forming elements (Sc, Y, and Lu) can be even higher ($D_c = 9$ mm) compared to the undoped alloy synthesized from low oxygen components. Therefore, we have demonstrated that it is feasible to produce BMG using low-purity constituents with REE-based oxygen scavengers. This bridges the gap between laboratory development and cost-effective commercial applications.

KRZYSZTOF PAJOR, DOROTA TYRAŁA, ŁUKASZ CIENIEK, and TOMASZ KOZIEŁ are with the Faculty of Metals Engineering and Industrial Computer Science, AGH University of Science and Technology, Al. Mickiewicza 30, 30-059 Kraków, Poland. Contact e-mail: kpajor@agh.edu.pl ŁUKASZ GONDEK is with the Faculty of Physics and Applied Computer Science, AGH University of Science and Technology, Al. Mickiewicza 30, 30-059 Kraków, Poland. PIOTR BŁYSKUN is with the Faculty of Material Science and Engineering, Warsaw University of Technology, Wołoska 141, 02-507 Warsaw, Poland.

Manuscript submitted March 10, 2023; accepted August 15, 2023.

Article published online August 30, 2023



<https://doi.org/10.1007/s11661-023-07176-9>
 © The Author(s) 2023

I. INTRODUCTION

OXYGEN contamination in Zr-based bulk metallic glasses (BMGs) has been the subject of scientific research for many years.^[1–3] It is well known that this impurity is the key limiting factor for wide application of BMGs, as it degrades their glass-forming ability (GFA) and mechanical properties.^[4–6] The most oxygen-sensitive GFA parameter is the critical diameter (D_c —maximum amorphous thickness), which has a logarithmic dependence.^[6] Therefore, high-purity components and strict casting conditions, such as vacuum systems and protective atmospheres, are required during BMG production, thus, generating high synthesis costs.

The vitrification of BMG alloys using commercial purity components is very difficult. The first approach was reported by Turnbull's group, where a 1 cm sample without crystalline products was obtained through the deoxidation of the $\text{Pd}_{40}\text{Ni}_{40}\text{P}_{20}$ alloy in a molten flux of dehydrated boron oxide.^[7] However, this procedure is complicated, since it involves multiple alloy remelting, together with the initially prepared high-purity B_2O_3 (preheated at 1000 °C for 36 hours in a palladium crucible to remove residual water). The remelting cycle temperatures had to be carefully selected to not exceed or go below the glass transition temperatures of the alloy and B_2O_3 , respectively. These very strict conditions make this method unsuitable for a wide range of applications.

Alternatively, Hydrogen Arc Melting (HAM) has been proposed as a method of deoxidizing BMGs.^[8] Increasing the hydrogen percentage in the gaseous mixture allowed to decrease the oxygen content in the alloy from 900 to 270 wt ppm. However, this method also has its limitations. Hydrogen can form gas bubbles in the as-cast alloys or be absorbed by the melt, affecting its glass-forming ability and the physical properties of

final product.^[8,9] The simplest approach for reducing oxygen impurities is doping with elements possessing higher affinity to oxygen compared to the constituent elements.

Due to the high Gibbs free energy of ZrO_2 formation ($-521.4 \text{ kJ mol}^{-1}$ per mole of oxygen at 25 °C^[10]), the ideal candidates are rare-earth elements (REEs), as most of them are characterized by even higher free energy of oxide formation (examples for investigated REE: $\text{Sc}_2\text{O}_3 - 606.5 \text{ kJ mol}^{-1}$, $\text{Y}_2\text{O}_3 - 605.5 \text{ kJ mol}^{-1}$, $\text{Lu}_2\text{O}_3 - 596.3 \text{ kJ mol}^{-1}$, $\text{Gd}_2\text{O}_3 - 577.4 \text{ kJ mol}^{-1}$, and $\text{Nd}_2\text{O}_3 - 573.7 \text{ kJ mol}^{-1}$).^[10] However, not all REEs can be easily used for various reasons, such as too low evaporating temperature (Sm, Eu, Yb), spontaneously combustion when exposed to air (Pr, Eu) or radioactivity (Pm). There are a lot literature reports on dealing with Zr-based BMG doping with Sc,^[11–13] Y,^[14–21] La,^[11,22] Ce,^[21–23] Pr,^[23] Nd,^[21,22,24] Gd,^[20–23] Tb,^[20,23] Dy,^[20,21] Ho,^[20] Er,^[15,20] Tm,^[20] Yb,^[20] and Lu.^[20,21,25] However, only two of the papers cited above gave a specific concentration of REE in relation to oxygen content, whereas other papers actually studied combined scavenging and alloying effects.^[11,12]

The use of an appropriate amount of REE for the doping of metallic glasses is of great importance. While the scavenging effect has a generally positive effect on glass-forming ability, the alloying effect can change the composition of the matrix, leading to partial crystallization during solidification. In addition, REEs are expensive materials due to limited availability and costly extraction and should, therefore, be used in strictly defined quantities.

In our previous work, we presented a novel approach of doping the ternary $\text{Zr}_{50}\text{Cu}_{40}\text{Al}_{10}$ glass-forming alloy with a known oxygen content and including contaminations originating from the REEs.^[26] The rare earths were selected based on the crystallographic structures of

their sesquioxides, which are stable in the temperature range of alloy synthesis: cubic (Sc_2O_3 , Y_2O_3 , and Lu_2O_3), hexagonal (Nd_2O_3), and with the polymorphic transition from monoclinic to cubic (Gd_2O_3).^[27] In this study, these aspects were studied in greater detail in the more complex quinary $\text{Zr}_{52.5}\text{Cu}_{17.9}\text{Ni}_{14.6}\text{Al}_{10}\text{Ti}_5$ alloy. As will be demonstrated, the effect of doping can differ significantly depending on the alloy system.

II. MATERIAL AND METHODS

The alloys of nominal composition (at. pct) $\text{Zr}_{52.5}\text{Cu}_{17.9}\text{Ni}_{14.6}\text{Al}_{10}\text{Ti}_5$ were prepared using high-purity elements (at least 99.99 wt pct) and two Zr metal purities: 99.95 wt pct (nominal oxygen level of 150 wt ppm) and 99.8 wt pct (nominal oxygen level of 1200 wt ppm). Depending on the Zr purity, the as-cast samples were designated as low oxygen (LO) and high oxygen (HO), respectively. The appropriate amount of rare-earth dopant necessary to scavenge all oxygen from the solution (including contamination coming from themselves, see procedure described in Reference 26) was calculated based on oxygen analysis in the HO variant. This was done *via* the inert gas fusion method (LECO RO 416 DR, ASTM E1409 standard) and the following REE-oxygen relations: stoichiometric (sesquioxide M_2O_3 —hereafter referred to as 2/3), double- (4/3), and triple-stoichiometric (6/3) (REE = Sc, Y, Lu, Gd, and Nd). Alloys were synthesized by means of arc melting in a high-purity Ti-gettered argon (6N) atmosphere and then suction cast into copper mold rod-shaped cavities (dia. 3 to 10 mm). The water cooling system temperature was set to 290 ± 1 K (17 ± 1 °C).^[28]

The microstructure observations, phase analysis, and thermal studies were carried out on samples taken from the central part of the as-cast alloys. The critical diameters (D_c) were determined based on scanning electron microscopy (SEM, FEI Nova NanoSEM 450) and X-ray diffraction (XRD, Panalytical Empyrean). The largest diameter of the alloys characterized by the absence of diffraction peaks and the presence of only trace amounts of crystals was considered to be D_c . The chemical composition was measured using energy-dispersive X-ray spectroscopy (EDX, EDAX Apollo X, Octane Elect Plus) and wavelength-dispersive X-ray spectroscopy (WDS, EDAX TEXS HP, Transition Element X-ray Spectrometer—High Precision) detectors installed within the SEM.

The GFA was studied using differential thermal analysis (DTA, Setaram Labsys) at a constant heating rate of 20 K/min in a protective argon (5N) gas flow of 20 ml/min. On the DTA curves, characteristic temperatures were determined: T_g —glass transition (inflection point according to ASTM E1356 standard), T_x —onset of crystallization, T_p —peak of crystallization, T_m —solidus, T_l —liquidus. Based on these values, the GFA indicators with the best coefficient of determination to the D_c were calculated: $\Delta T_{xg} = T_x - T_g$, $T_{rg} = T_g/T_l$, and $\delta = T_x/(T_l - T_g)$.

III. RESULTS AND DISCUSSION

A. Oxygen Contamination and Characterization of Reference Alloys

The oxygen level in the reference (undoped) LO and HO variants was measured to be 565 ± 58 and 957 ± 62 wt ppm, respectively. It means that oxygen contamination in the LO alloy originates not only from Zr (the nominal oxygen concentration of 150 wt ppm according to the producer certificate), but also from other components (probably Ni and Ti). These oxygen levels allowed to obtain $D_c = 6$ mm for LO alloys and below 3 mm for the HO alloy (XRD diffraction patterns shown in Figure 1). Casting rods with a smaller diameter (*e.g.*, 1 or 2 mm) is problematic due to the high cooling rate in a copper mold, which leads to clogging below the inlet and the formation of many casting defects. Liu *et al.*^[29] achieved 7 mm glassy samples of the $\text{Zr}_{52.5}\text{Cu}_{17.9}\text{Ni}_{14.6}\text{Al}_{10}\text{Ti}_5$ alloy prepared from an extremely high-purity Zr crystal bar with oxygen content of 12.3 at. ppm (2.2 wt ppm). Kündig *et al.*^[11] obtained $D_c = 4$ mm in this alloy with oxygen content in the range of 100–120 wt ppm, while $D_c = 6$ mm for 90 wt ppm. More comprehensive studies were carried out by Campos Neto *et al.*,^[30] who synthesized several alloys with oxygen levels between 200 and 1250 wt ppm. According to the criterion of the 5 pct threshold crystalline areas, they obtained 6 mm for 500 wt ppm. This means that the oxygen level is only one factor affecting glass-forming ability, and the effect of processing route should not be neglected. As we showed in Reference 28, the water cooling system (WCS) temperature dramatically affects the axial cooling rate (CR) in the casting process. This effect is more evident in the case of smaller diameters. For example, axial CR of a 3 mm cast is 212 and 177 K/s for WCS temperatures of 290 K (17 °C) and 295 K (22 °C), respectively. Similarly, for a 5 mm cast sample, the axial CR is 65 and 55 K/s, respectively. Therefore, ensuring proper casting conditions is as important as using high-purity constituent elements.

As mentioned previously, the nominal additions of REEs were calculated based on HO variant analysis, and are summarized in Table I, along with the actual added REE amounts.

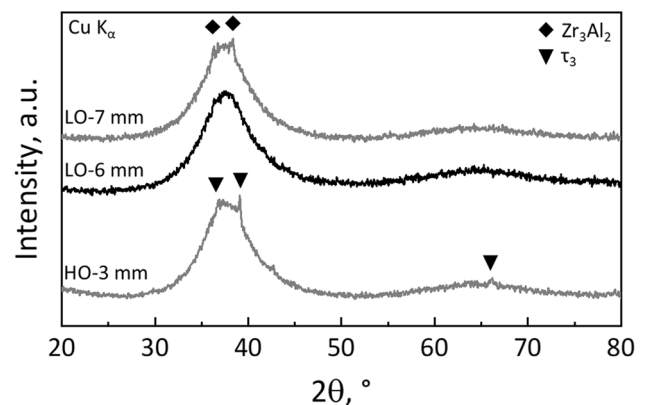


Fig. 1—X-ray diffraction patterns (amorphous—black, partially crystalline—gray) of reference LO and HO alloys.

Table I. Nominal and Actual Rare-Earth Additions in $(\text{Zr}_{52.5}\text{Cu}_{17.9}\text{Ni}_{14.6}\text{Al}_{10}\text{Ti}_5)_{100-x}\text{REE}_x$ Alloy (HO Variant)

REE-to-Oxygen Ratio	Nominal REEs Additions (At. Pct)	Actual REEs Additions (At. Pct)				
		Sc	Y	Lu	Gd	Nd
2/3	0.290	0.292	0.307	0.310	0.290	0.333
4/3	0.580	0.588	0.653	0.667	0.581	0.780
6/3	0.869	0.888	1.045	1.082	0.873	1.408

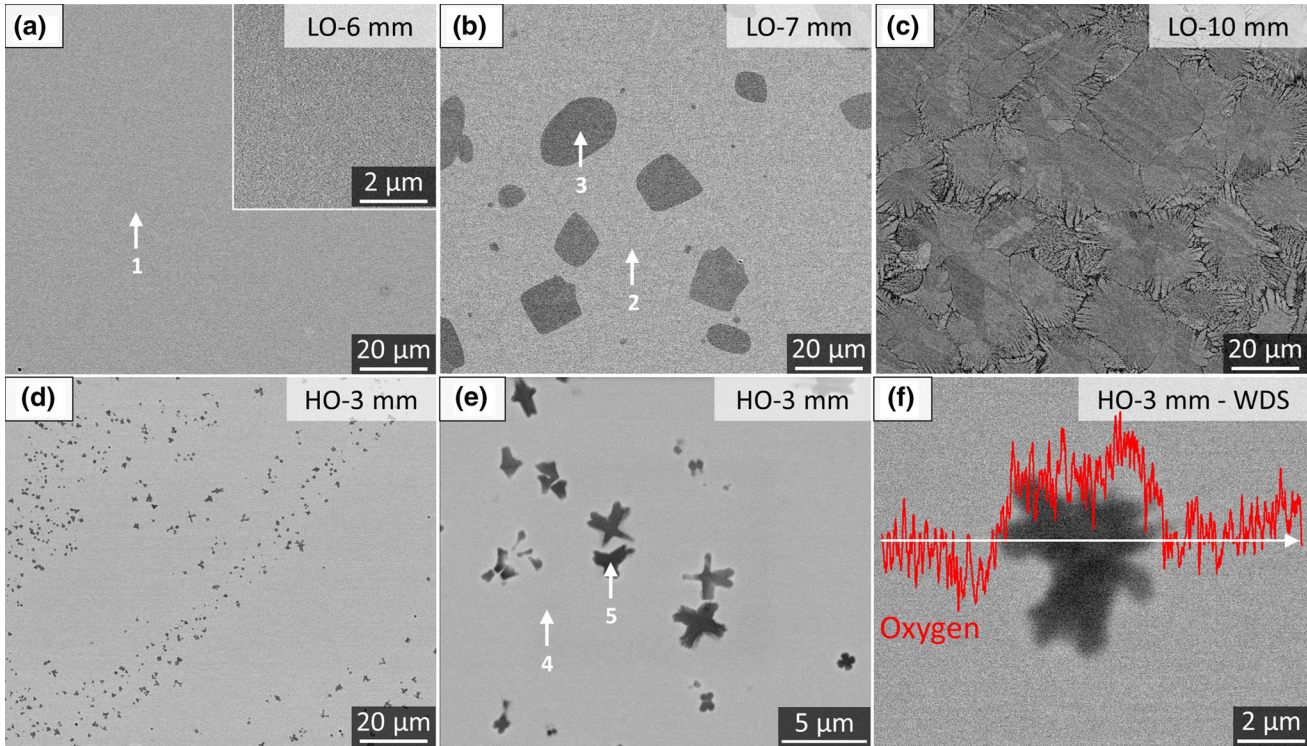


Fig. 2—Microstructures (SEM-BSE) of the reference alloys. Top row shows 6-mm (a), 7-mm (b), and 10-mm (c) diameter LO samples. Bottom row (d through f) shows the 3-mm diameter HO sample. (f) shows the WDS line scan of oxygen content. White arrows mark areas of EDX analysis (results given in Table II).

Figure 2 shows selected SEM-backscattered electron (BSE) images of the reference (undoped) LO and HO alloys. Microscopic observations of 6- and 7-mm diameter LO samples confirmed the XRD results. A featureless appearance was observed only for the 6-mm dia. sample [Figure 2(a)], whereas in the central part of the 7-mm dia. sample [Figure 2(b)], several crystallites can be seen, which were also detected in the XRD. SEM-EDX analysis indicates no difference between the matrix (Figure 2; Table II, spot 2) and the crystalline areas (spot 3). This is probably related to the polymorphous transformation, *i.e.*, crystallization without chemical composition change. To identify this phase, an additional 10-mm diameter sample was cast, which lead to increased peak intensity (Figure 3). According to database records (mp-13470 number), the lattice parameters of Zr_3Al_2 are $a = b = 7.65 \text{ \AA}$, $c = 6.98 \text{ \AA}$.^[31] In the literature, a variety of lattice parameters of tetragonal Zr_3Al_2 -like phases have been reported. Campos

Table II. Results of SEM-EDX Semiquantitative Analysis of References Alloys (Fig. 2), At. Pct

Alloy	Spot	Zr	Cu	Ni	Al	Ti	Phase
LO-6 mm	1	51.3	17.4	13.7	12.8	4.8	matrix
LO-7 mm	2	51.4	17.1	13.5	13.4	4.6	matrix
LO-7 mm	3	52.0	17.0	13.5	13.1	4.4	Zr_3Al_2
HO-3 mm	4	51.4	17.4	13.3	13.1	4.9	matrix
HO-3 mm	5	49.5	16.8	9.9	19.9	3.9	τ_3

Neto *et al.*^[30] estimated the parameters of this phase in $\text{Zr}_{52.5}\text{Cu}_{17.9}\text{Ni}_{14.6}\text{Al}_{10}\text{Ti}_5$ alloy as $a = 7.40 \text{ \AA}$, $c = 6.66 \text{ \AA}$. In turn, Xing *et al.*^[32] identified Zr_3Al_2 in $\text{Zr}_{69.5}\text{Cu}_{12}\text{Ni}_{11}\text{Al}_{7.5}$ with $a = 7.88 \text{ \AA}$, $c = 7.10 \text{ \AA}$. The difference in lattice parameters results from the supersaturation of this phase by various elements during polymorphous crystallization. The stoichiometric chemical composition of Zr_3Al_2 is 60 pct Zr/40 pct Al, while in the investigated

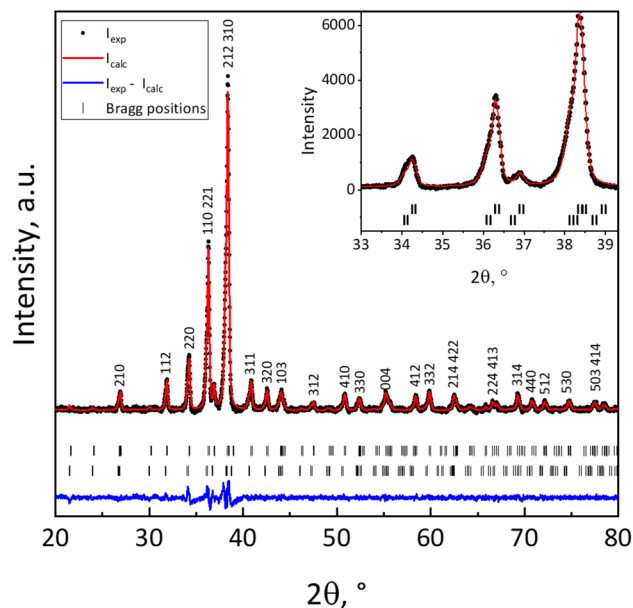


Fig. 3—Le Bail refinement of the XRD data of the 10-mm diameter LO alloy sample to analyze the Zr_3Al_2 phase ($P4_2/mnm$), as discussed in Section III-A.

alloy, this ratio is 52.5 pct Zr/10 pct Al. Other components can replace Zr and Al, having metallic radii of 160 pm and 143 pm, respectively. The metallic radii of Cu and Ni (total concentration of both elements in the investigated alloy is 32.5 pct) are 128 pm and 124 pm, respectively.^[33] Significant differences in atomic radii of constituents affect the parameters of the unit cell, leading to diffraction peak shifting relative to its reference positions in database. In our case, Le Bail refinement revealed that two Zr_3Al_2 -like phases (space group $P4_2/mnm$) with slightly different lattice parameters could have contributed to the diffraction pattern. The parameters are $a = 7.4011(1)$ Å, $c = 6.6514(1)$ Å for the main phase (first row of Bragg reflections in Figure 3), and $a = 7.4405(1)$ Å, $c = 6.6886(1)$ Å for the secondary phase (second row of Bragg reflections in Figure 3). The necessity of using two phases is evident after inspecting the reflection shapes between 30 and 40 deg of 2θ , as presented in Figure 3's inset. This finding is in line with previously discussed literature data.

SEM-BSE images of the 3-mm diameter cast HO alloy rod are shown in Figures 2(d) through (f). In this case, a small amount of dendritic phase is randomly dispersed across the transverse cross section. Such inclusions in Zr-Cu-Al-(Ni, Ti) alloys with increased oxygen levels are often interpreted as $NiZr_2$ or Zr_4Ni_2O phases.^[34,35] More convincing interpretation was presented in the last few years, referred to the τ_3 phase ($Zr_{51}Cu_{28}Al_{21}$) that is associated with oxygen impurities.^[4,26,36–38] According to Zhou *et al.*,^[38] the oxygen contamination in the alloy is responsible for the stabilization of this phase and, depending on the level, affects its morphology, volume fraction, and oxygen content in the phase itself. The authors showed that very low oxygen amounts (86 wt ppm) allowed obtaining a

precipitate-free casting in the $Zr_{50.75}(Cu_{90}Ni_{10})_{40.25}Al_{10}$ alloy, while at 350 wt ppm, they observed small precipitates of regular shapes. A further increase in the oxygen level increased the size and complexity of the τ_3 phase, reaching a maximum at 830 wt ppm, above which no significant changes were found. The morphology of τ_3 takes on a dendritic shape, which suggests its formation in liquid phase. Our previous work confirmed this statement, where the τ_3 was stable far beyond the melting temperature of the $Zr_{50}Cu_{40}Al_{10}$ alloy. In the experiments carried out by Zhou, the lattice parameter of the τ_3 phase (space group $Fm\bar{3}m$) depended on the oxygen content and was calculated to be 11.895, 11.898, 11.907, and 11.904 Å for 350, 660, 830, and 1900 wt ppm, respectively.^[38] The results presented in this work, *i.e.*, morphology (Figures 2(d), (e)), chemical composition (Table II, spot 5) and WDS line scan [Figure 2(f)] all indicate towards the formation of the τ_3 phase.

B. Alloys Doped with Cubic Oxide-Forming REEs

Our previous investigations of the $Zr_{50}Cu_{40}Al_{10}$ alloy with a high oxygen level showed that the best scavenging effect was obtained when doping with cubic oxide-forming REEs (Sc, Y, and Lu).^[26] The largest critical diameter was determined in alloys doped with Y, with the D_c increased from < 3 mm up to 8 mm for the 6/3 variant, whereas Sc and Lu only allowed for D_c values of 5 mm and 6 mm, respectively. In this study, all cubic sesquioxide-forming elements increased the glass-forming ability up to 9 mm, although some differences can be seen.

Figure 4 shows the X-ray diffraction patterns of rod samples with diameters corresponding to their D_c value, as well as $D_c + 1$ mm along with representative SEM-BSE images. The highest critical diameter value ($D_c = 9$ mm) for Sc and Y additions was obtained in a double-stoichiometric (4/3) variant with respect to the measured oxygen content. The main crystalline phase detected in the samples with diameters exceeding the critical diameter value ($D_c + 1$ mm) was the Zr_3Al_2 phase, observed as dark contrast areas (Figure 4; Table III, spots 3 and 6). However, some τ_3 phase was also observed in the case of the HO 2/3Sc variant. This means that oxygen was not fully bound by the dopant, and the minimum Sc concentration necessary to scavenge this impurity in this alloy is higher than that determined by the single stoichiometric addition.

Interestingly, the most promising results were obtained for Lu additions, achieving $D_c = 9$ mm for all variants. It is worth noting that the critical diameter is determined based on the discrete method, with the real D_c being in the range of 9 to 10 mm. When studying the diffraction pattern in more detail, a drop in peak intensity is observed with increasing Lu content indicating that the actual D_c of these alloys slightly increased. Therefore, after binding all oxygen from the alloy, Lu has a positive effect on the alloy's glass-forming ability. A similar effect was reported in our previous work ($Zr_{50}Cu_{40}Al_{10}$), as well as Deng *et al.*^[21] ($Cu_{47}Zr_{45}Al_8$) and Zhou *et al.*^[25] ($Zr_{50}Ti_2Cu_{38}Al_{10}$);

however, ternary and quaternary systems are simpler compared to the studied $Zr_{52.5}Cu_{17.9}Ni_{14.6}Al_{10}Ti_5$ alloy. The 10-mm dia. HO 2/3Lu alloy possessed the largest number of high intensity peaks and a weak amorphous “halo.” This is due to the alloy’s high degree of crystallinity, which, apart from the Zr_3Al_2 phase and τ_3 inclusions, also contains $CuZr_2$ and Zr_6NiAl_2 phases. These two phases are most likely the decomposition products of the non-equilibrium (saturated with other elements) Zr_3Al_2 phase formed due to insufficient cooling rates during solidification, seen as precipitation inside Zr_3Al_2 (Figure 4, inset of HO 6/3Lu variant).^[32] Furthermore, in all patterns, there is a small peak visible at $2\theta = 30^\circ$ originating from the Lu_2O_3 phase, despite the volume fraction of oxides being far below 1 pct. No additional phases were observed on the microstructures, even in the HO 4/3Lu sample (higher noise on XRD pattern); therefore, these samples were treated as amorphous. Compared to scandia and yttria, lutetia on SEM-BSE images has a white contrast due to the high atomic number of Lu. The chemical composition of lutetium oxide (Figure 3; Table III, spot 8) does not include Al, due to the overlapping energy of the

characteristic radiation of lutetium and aluminum (Al $K_\alpha = 1.486$ keV, Lu $M_\alpha = 1.581$ keV).

Despite the high oxygen level in the $Zr_{52.5}Cu_{17.9}Ni_{14.6}Al_{10}Ti_5$ alloy, the critical diameter can be significantly increased, even exceeding the value obtained in the LO alloy, by doping it with cubic oxide-forming

Table III. Results of SEM-EDX Semiquantitative Analysis of HO Alloys Doped with Sc, Y, and Lu (Fig. 3), At. Pct

Spot	Zr	Cu	Ni	Al	Ti	REE	O	Phase
1	5.2	1.0	0.7	0.6	0.0	40.4	52.1	Sc_2O_3
2	49.9	16.8	9.4	20.1	3.8	—	—	τ_3
3	51.9	17.4	13.2	13.0	4.5	—	—	Zr_3Al_2
4	51.7	17.2	13.5	12.9	4.7	—	—	matrix
5	0.0	1.6	1.3	4.2	0.5	72.4	20.0	Y_2O_3
6	51.4	16.6	13.9	12.8	5.3	—	—	Zr_3Al_2
7	51.6	17.0	13.6	12.9	4.9	—	—	matrix
8	5.4	2.8	8.0	—	0.5	36.5	46.8	Lu_2O_3
9	48.7	17.2	9.6	20.1	4.4	—	—	τ_3
10	50.3	17.5	14.0	13.7	4.5	—	—	eutectoid
11	51.2	17.2	13.6	13.2	4.8	—	—	Zr_3Al_2
12	50.3	17.2	14.0	13.7	4.8	—	—	matrix

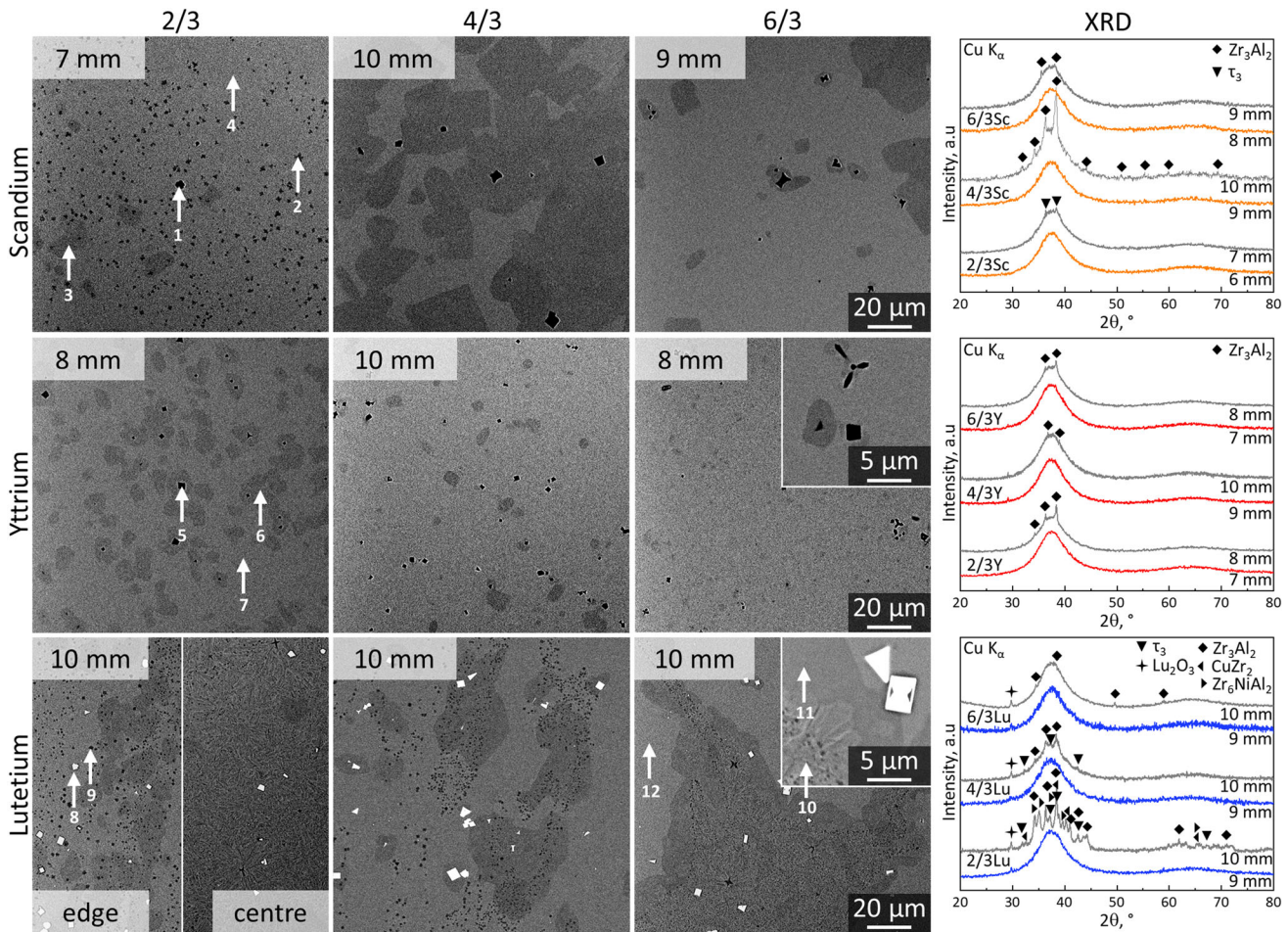


Fig. 4—Microstructures (SEM-BSE) and the XRD patterns of the HO alloy doped with Sc, Y, and Lu in stoichiometric (2/3), double-stoichiometric (4/3), and triple-stoichiometric (6/3) REE-to-oxygen ratios. White arrows mark areas of EDX analysis (results given in Table III).

REEs (6 mm for 565 ± 58 wt ppm of oxygen in LO variant vs. 9 mm for 957 ± 62 wt ppm variant doped with REE forming cubic sesquioxides). As we pointed out in Section III–A, D_c strongly depends on the oxygen impurity, which means that proper doping of the LO variant should also increase the critical diameter to 9 mm, but it was not the case in the present study.

C. Alloy Doped with Transition (Monoclinic to Cubic) Oxide-Forming REE

The Gd_2O_3 oxide is characterized by a polymorphous transformation from monoclinic to cubic at 1425 K (1152 °C) during cooling; however, the presence of the C-type structure for Gd_2O_3 at low temperatures is still unclear.^[27] In our previous study, STEM analysis showed a BBC ($Ia\bar{3}$) structure, and no evidence of transformation was found.^[26] However, a change was seen in the element distribution, *i.e.*, apart from the oxides, gadolinium was also detected in the amorphous matrix. A D_c of 3 mm was obtained for the 6/3 variant, meaning that the partial dissolution of Gd inhibited the

scavenging effect.^[26] Here, Gd additions led to D_c values of 6 mm for all variants (Figure 5), which corresponds to the value obtained in the LO reference alloy.

The τ_3 phase was observed in the microstructure of 2/3 and 4/3 variant samples, with diameters exceeding the critical diameter value ($D_c + 1$ mm), where in the latter, it was finely dispersed and the dominant crystalline phase (inset in Figure 5). As they were so fine, it was not possible to quantitatively analyze their chemical composition; however, it was possible to track the change in element distribution (Figure 5; Table IV, spot 2).

With increasing Gd concentration, more Zr_3Al_2 phase formed at the expense of τ_3 . In sample HO 6/3Gd (dia. 7 mm), no traces of τ_3 phase were detected, neither in the XRD pattern nor during microstructural observations.

D. Alloy Doped with Hexagonal Oxide-Forming REE

Among all studied rare-earth elements, neodymium (oxide of which crystallizes in a hexagonal structure) showed the lowest effectiveness in improving the glass-forming ability. The maximum value of critical

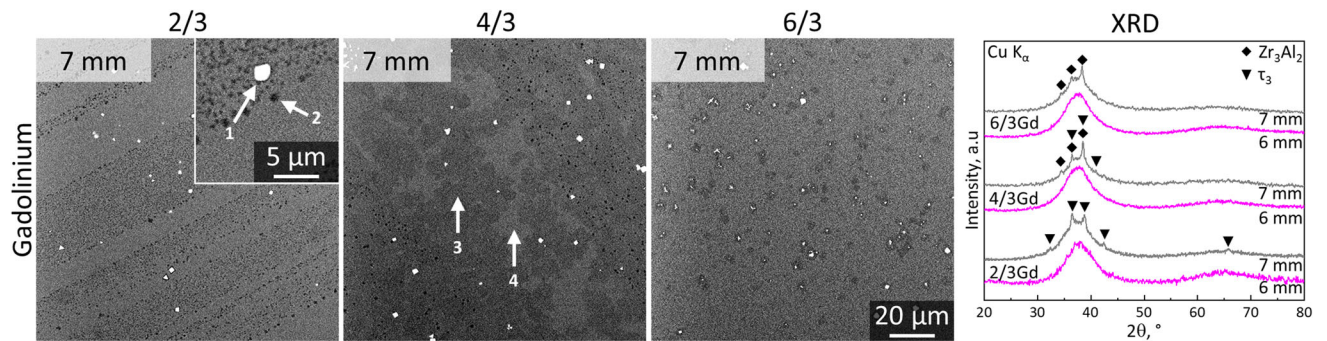


Fig. 5—Microstructures (SEM-BSE) and XRD patterns of the HO alloy doped with Gd in stoichiometric (2/3), double- (4/3), and triple-stoichiometric (6/3) REE-to-oxygen ratios. White arrows mark areas of EDX analysis (results given in Table IV).

Table IV. Results of SEM-EDX Semiquantitative Analysis of HO Alloys Doped with Gd (Fig. 4), At. Pct

Spot	Zr	Cu	Ni	Al	Ti	RE	O	Phase
1	18.3	6.1	4.4	4.0	1.3	21.6	44.3	Gd_2O_3
2	49.5	17.0	10.2	18.7	4.6	—	—	τ_3
3	51.6	17.3	13.8	12.8	4.5	—	—	Zr_3Al_2
4	51.9	17.4	13.8	12.8	4.6	—	—	matrix

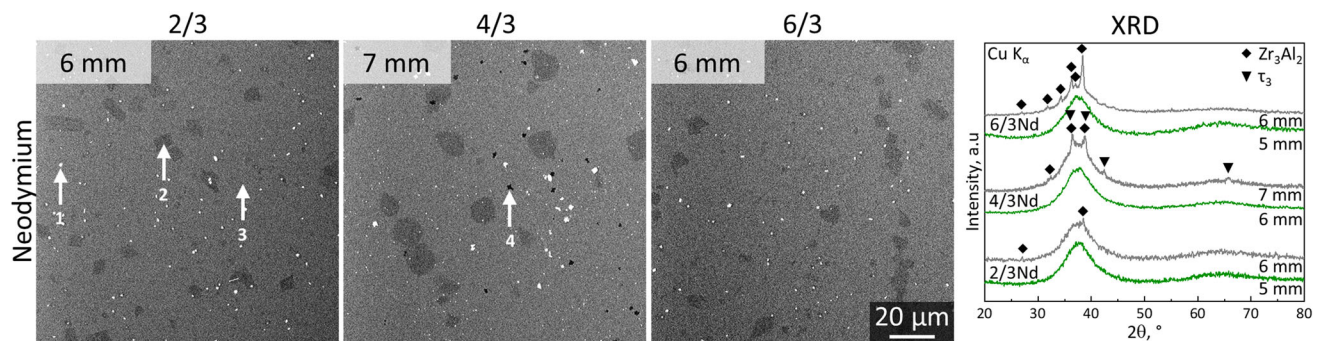


Fig. 6—Microstructures (SEM-BSE) and diffraction patterns (XRD) of the HO alloy doped with Nd in stoichiometric (2/3), double- (4/3), and triple-stoichiometric (6/3) REE-to-oxygen ratios. White arrows mark areas of EDX analysis (results given in Table V).

Table V. Results of SEM-EDX Semiquantitative Analysis of HO Alloys Doped with Nd (Fig. 5), At. Pct

Spot	Zr	Cu	Ni	Al	Ti	REE	O	Phase
1	35.7	9.3	7.2	11.2	2.7	25.0	8.9	Nd ₂ O ₃
2	51.2	17.0	15.2	13.1	3.5	—	—	Zr ₃ Al ₂
3	50.8	17.7	13.9	12.8	4.8	—	—	matrix
4	50.0	16.3	9.0	21.1	3.6	—	—	τ ₃

diameter ($D_c = 6$ mm) was obtained only in variant 4/3. It is interesting that, unlike Gd, the τ_3 phase was almost completely eliminated already in variant 2/3, where its presence was found only in some areas of sample HO 4/3Nd (Figure 6; Table V, spot 4). Due to the small oxide size, the signal collected during EDX analysis also included matrix (Figure 5; Table V, spot 1). Apart from oxides, the dominant crystalline phase was Zr₃Al₂ with the chemical composition corresponding to that of the matrix (Figure 6; Table V, spots 2 and 3).

E. The Critical Diameter Comparison

A summary of the D_c values determined in the reference (LO and HO) and doped alloys is shown in Figure 7. In general, the highest D_c was obtained for double-stoichiometric additions (variant 4/3). However, for the Zr₅₀Cu₄₀Al₁₀ alloy, we observed continuous

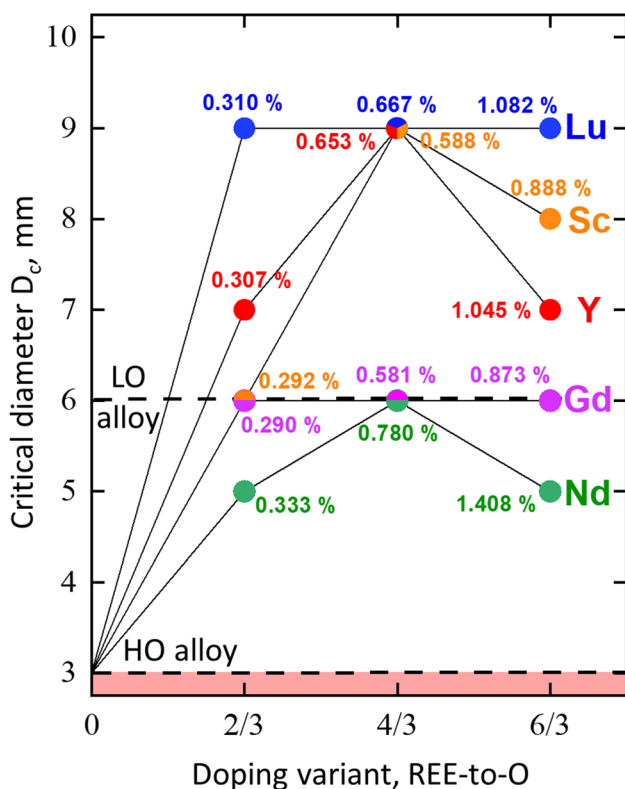


Fig. 7—Dependence of D_c on the Sc, Y, Lu, Nd, and Gd doping variant of Zr_{52.5}Cu_{17.9}Ni_{14.6}Al₁₀Ti₅ (the real REEs concentration according to Table I, at. pct). Dashed lines represent reference LO and HO alloys.

growth.^[26] This may be influenced by the initial glass-forming ability of both reference alloys. Zr_{52.5}Cu_{17.9}Ni_{14.6}Al₁₀Ti₅ contains 5 elements with different metallic radii and heat of mixing between them, so a slight change in chemical composition can easily disturb this fragile balance. Partial dissolution of rare earths in the liquid changes the chemical composition, thus, affecting its vitrification. This is especially evident in the case of Nd and Gd, which were observed in the matrix.^[26] In comparison, the 3-component alloy has not reached its potential, and dissolution of an additional element can still improve its glass-forming ability. These considerations show that the presented issues are very complex and difficult to solve unambiguously.

F. Thermal Analysis

Figure 8 shows DTA curves performed on the highest glassy diameter samples at a heating rate of 20 K min⁻¹. Characteristic temperatures and selected GFA indicators are listed in Table VI. The undoped LO alloy is characterized by a glass transition temperature of 676 K (403 °C), followed by two exothermic peaks (crystallization events) starting at 708 K (435 °C). The amorphous phase crystallizes in two stages; however, thermal effects overlap at this heating rate, leading to the two peaks merging.^[39] Although the critical diameter of this alloy is 6 mm, the obtained supercooled liquid region ΔT_{xg} was only 32 K. A similar thermal behavior was noticed for the HO variant with a sample size of 3 mm; however, the measured ΔT_{xg} value was lower (28 K). No additional thermal effects were observed between crystallization and melting, indicating that the crystallization products are stable up to the solidus temperature. The melting range, *i.e.*, the difference between the solidus and liquidus temperatures, was significantly higher for the HO variant (54 K vs. 42 K).

The thermal behavior of the HO alloys doped with rare-earth elements did not cause significant change of the characteristic temperatures. In our previous work, doping the ternary Zr₅₀Cu₄₀Al₁₀ alloy with the same REEs leads to a visible change in these temperatures and consequently GFA parameters.^[26] Similar observations were made in other works.^[12,15,21,22] In this study, the T_g temperature of all doped alloys decreased with increasing rare-earth concentration, reaching values close to those of the LO alloy. A similar relationship was also found with respect to the T_x temperature; therefore, the value of ΔT_{xg} slightly increased in all cases, exceeding in some variants even that obtained in the low oxygen alloy.

No other transformations were observed between the crystallization and melting processes in doped alloys, except at higher concentrations of neodymium (Figure 8f). There, an additional exothermic effect was observed around 873 K (600 °C). Additional X-ray or neutron diffraction experiments at elevated temperatures would be necessary to identify this type of transformation. The temperature that significantly affects the GFA is the liquidus temperature T_l . Only the addition of yttrium caused a pronounced decrease in T_l , even below that obtained in the LO alloy. An interesting observation is the behavior of Y and Gd, the

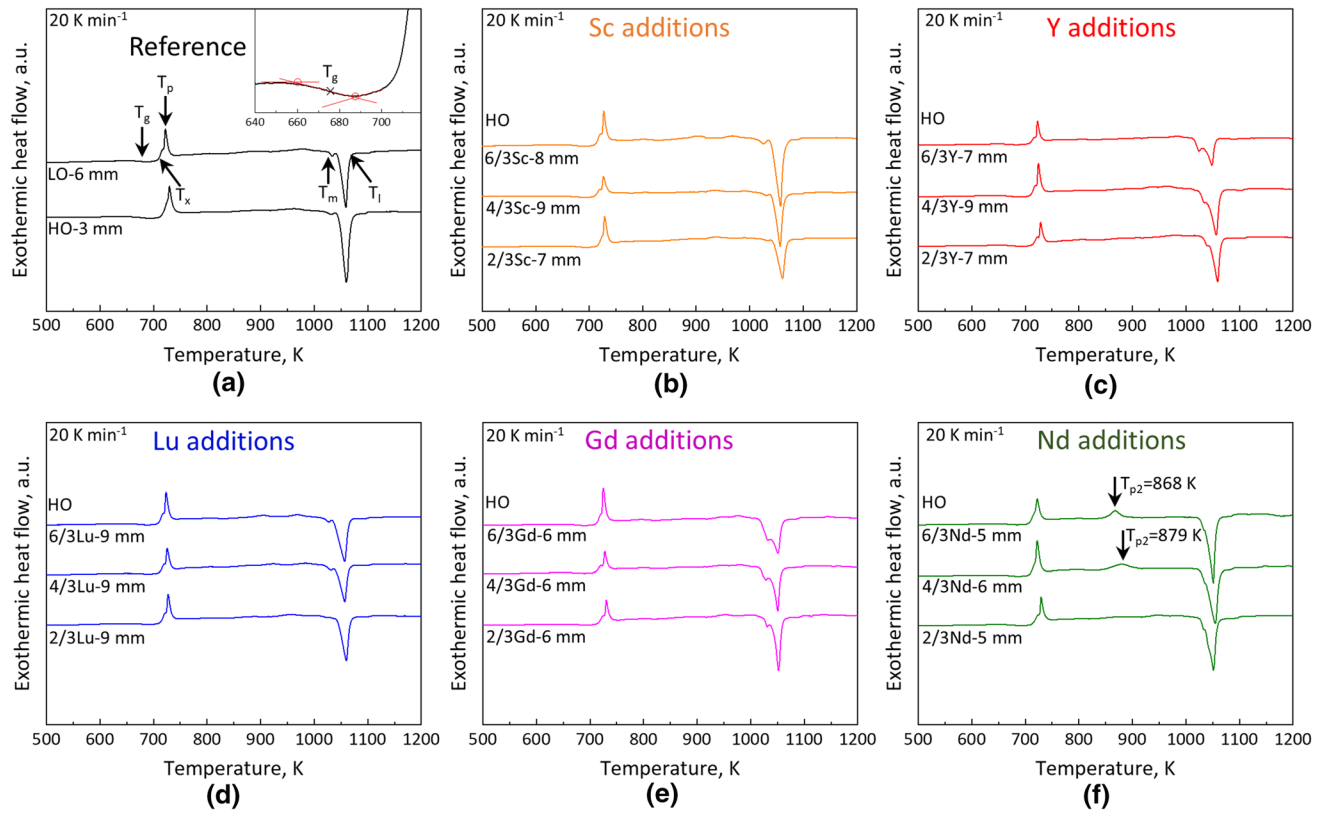


Fig. 8—DTA curves of the reference LO and HO alloys (a), HO alloy doped with Sc (b), Y (c), Lu (d), Gd (e), and Nd (f). Characteristic temperatures: T_g —glass transition (found according to ASTM E1356 standard, see inset), T_x —crystallization onset, T_p —peak of crystallization, T_m —solidus, T_l —liquidus.

Table VI. Characteristic Temperatures and GFA Indicators of Reference (LO and HO) and Doped Alloys; $\Delta T_{xg} = T_x - T_g$, $T_{rg} = T_g/T_l$, $\delta = T_x/(T_l - T_g)$

Alloy	D , mm	Characteristic Temperatures, K					GFA Indicators		
		T_g	T_x	T_p	T_m	T_l	ΔT_{xg}	T_{rg}	δ
LO	6	676	708	722	1027	1069	32 K	0.632	1.802
HO	3	685	713	730	1021	1075	28 K	0.637	1.828
HO2/3Sc	6	684	715	729	1027	1075	31 K	0.636	1.824
HO4/3Sc	9	674	710	727	1021	1075	36 K	0.627	1.771
HO6/3Sc	8	679	711	727	1013	1076	32 K	0.631	1.791
HO2/3Y	7	679	713	729	1030	1072	34 K	0.633	1.814
HO4/3Y	9	675	710	724	1025	1068	35 K	0.632	1.807
HO6/3Y	7	673	706	722	1015	1060	33 K	0.635	1.824
HO2/3Lu	9	678	712	727	1030	1074	34 K	0.631	1.798
HO4/3Lu	9	674	710	725	1021	1070	36 K	0.630	1.793
HO6/3Lu	9	673	709	723	1019	1070	36 K	0.629	1.786
HO2/3Gd	6	677	710	731	1024	1066	33 K	0.635	1.825
HO4/3Gd	6	675	710	728	1017	1064	35 K	0.634	1.825
HO6/3Gd	6	674	711	725	1017	1064	37 K	0.633	1.823
HO2/3Nd	5	680	711	730	1025	1066	31 K	0.638	1.842
HO4/3Nd	6	673	707	722	1025	1069	34 K	0.630	1.785
HO6/3Nd	5	674	706	722	1024	1064	32 K	0.633	1.810

Alloys with critical diameter below 3 mm is given in bold

addition of which resulted in a significant extension of the melting effect.

Based on the characteristic temperatures (T_g , T_x , and T_l), different GFA indicators and their coefficient of determination (COD) to the critical diameters were

calculated.^[40,41] Among 21 indicators, the best correlation was obtained for ΔT_{xg} (COD = 0.308), T_{rg} (COD = 0.513), and δ (COD = 0.452). The differences in T_g and T_x temperatures were not significant; therefore, their impact on the GFA indicators was only

slight. Similar observations were made by Campos Neto *et al.*,^[30] who in the same alloy found a narrowing of the ΔT_{Xg} range with increasing oxygen content. The relationship between D_c and GFA indicators is convergent within one rare earth; however, they are not comparable between alloys doped with different REEs. For example, the highest critical diameter (9 mm) was obtained for HO 4/3Sc, HO 4/3Y, and all Lu variants for which the T_{rg} indicator was $0.627 \div 0.632$, while higher values ($0.633 \div 0.635$) were obtained for alloys doped with Gd which exhibited lower D_c .

IV. SUMMARY AND CONCLUSIONS

In the present work, we presented the influence of Sc, Y, Lu, Nd, and Gd dopants on the glass-forming ability (expressed by the critical diameter and calorimetric criteria) of the $\text{Zr}_{52.5}\text{Cu}_{17.9}\text{Ni}_{14.6}\text{Al}_{10}\text{Ti}_5$ alloy containing 957 ± 62 wt ppm of oxygen. Our results conclusively show the significant benefit of REEs microdopants on GFA, allowing this group of materials to be taken out of the domain of basic research domain and limited applications. In the light of the results presented and their discussion, the following conclusions can be drawn:

- (1) The critical diameter for glass formation in the $\text{Zr}_{52.5}\text{Cu}_{17.9}\text{Ni}_{14.6}\text{Al}_{10}\text{Ti}_5$ alloy strongly depends on the level of oxygen impurities, here 565 ± 58 and 957 ± 62 wt ppm, and was determined as 6 mm and below 3 mm, respectively.
- (2) Doping the high oxygen variant with rare-earth elements allowed to obtain D_c values exceeding those obtained in the low oxygen variant.
- (3) Rare earths forming cubic sesquioxides (Sc_2O_3 , Y_2O_3 , and Lu_2O_3) are the best oxygen scavengers allowing to obtain the highest critical diameter value of 9 mm.
- (4) Despite the weak scavenging effect of Gd and Nd, the critical diameter increased to 6 mm.
- (5) The greatest critical diameters were generally reached when using a double-stoichiometric REE-to-oxygen ratio, which corresponds to a nominal concentration of 0.580 at. pct of REE. Further increasing the concentration had no positive effect on D_c and in some cases even caused a decrease (Sc, Y, and Nd).
- (6) Calorimetric indicators of glass-forming ability can be used only in limited cases. Most of the indicators showed weak or no correlation with the critical diameters in the studied alloy.

ACKNOWLEDGMENTS

This work was financially supported by the Ministry of Science and Higher Education Republic of Poland under Contract No. 16.16.110.663.

CONFLICT OF INTEREST

On behalf of all authors, the corresponding author states that there is no conflict of interest.

OPEN ACCESS

This article is licensed under a Creative Commons Attribution 4.0 International License, which permits use, sharing, adaptation, distribution and reproduction in any medium or format, as long as you give appropriate credit to the original author(s) and the source, provide a link to the Creative Commons licence, and indicate if changes were made. The images or other third party material in this article are included in the article's Creative Commons licence, unless indicated otherwise in a credit line to the material. If material is not included in the article's Creative Commons licence and your intended use is not permitted by statutory regulation or exceeds the permitted use, you will need to obtain permission directly from the copyright holder. To view a copy of this licence, visit <http://creativecommons.org/licenses/by/4.0/>.

REFERENCES

1. J. Eckert, N. Mattern, M. Zinkevitch, and M. Seidel: *Mater. Trans. JIM*, 1998, vol. 39, pp. 623–32.
2. K. Pajor, T. Kozieł, G. Cios, P. Blyskun, P. Bała, and A. Zielińska-Lipiec: *J. Non. Cryst. Solids*, 2018, vol. 496, pp. 42–47.
3. C.A. Teixeira, R.V. da Silva, L.T. Pereira, and M.F. de Oliveira: *J. Non. Cryst. Solids*, 2020, vol. 535, 119966.
4. Y. Yokoyama, T. Shinohara, K. Fukaura, and A. Inoue: *Mater. Trans.*, 2004, vol. 45, pp. 1819–23.
5. C.A. Schuh, T.C. Hufnagel, and U. Ramamurty: *Acta Mater.*, 2007, vol. 55, pp. 4067–4109.
6. P. Blyskun, P. Maj, T. Kozieł, K. Pajor, and T. Kulik: *J. Non-Cryst. Solids J.*, 2019, vol. 509, pp. 80–87.
7. H.W. Kui, A.L. Greer, and D. Turnbull: *Appl. Phys. Lett.*, 1984, vol. 45, pp. 615–16.
8. F. Dong, Y. Su, L. Luo, L. Wang, S. Wang, J. Guo, and H. Fu: *Mater. Lett.*, 2012, vol. 83, pp. 1–3.
9. D. Granata, E. Fischer, and J.F. Löffler: *Acta Mater.*, 2015, vol. 99, pp. 415–21.
10. R.A. Robie, B.S. Hemingway, and J.R. Fisher: *Thermodynamic Properties of Minerals and Related Substances at 298.15K and 1 Bar Pressure and at Higher Temperatures*, United States Government Printing Office, Washington, 1978.
11. A.A. Kündig, D. Lepori, A.J. Perry, S. Rossmann, A. Blatter, A. Dommann, and P.J. Uggowitzer: *Mater. Trans.*, 2002, vol. 43, pp. 3206–10.
12. F. Jiang, Z.J. Wang, Z.B. Zhang, and J. Sun: *Scr. Mater.*, 2005, vol. 53, pp. 487–91.
13. H.-P. Cui, W.-D. Zhang, and C.-L. Song: *Chin. J. Mech. Eng.* <https://doi.org/10.21203/rs.3.rs-349393/v1>.
14. D. Xu, G. Duan, and W.L. Johnson: *Phys. Rev. Lett.*, 2004, vol. 92, pp. 1–4.
15. J. Luo, H. Duan, C. Ma, S. Pang, and T. Zhang: *Mater. Trans.*, 2006, vol. 47, pp. 450–53.
16. J. Chen, Y. Zhang, J.P. He, K.F. Yao, B.C. Wei, and G.L. Chen: *Scr. Mater.*, 2006, vol. 54, pp. 1351–55.
17. K. Zhou, Y. Liu, S. Pang, and T. Zhang: *J. Alloys Compd.*, 2016, vol. 656, pp. 389–94.
18. J. Zhu, C. Wang, J. Han, S. Yang, G. Xie, H. Jiang, Y. Chen, and X. Liu: *Intermetallics*, 2018, vol. 92, pp. 55–61.
19. S. Lu, S. Sun, K. Li, H. Li, X. Huang, and G. Tu: *J. Alloys Compd.*, 2019, vol. 799, pp. 501–12.

20. Q. Hu, M.W. Fu, and X.R. Zeng: *Mater. Des.*, 2014, vol. 64, pp. 301–06.
21. L. Deng, B. Zhou, H. Yang, X. Jiang, B. Jiang, and X. Zhang: *J. Alloys Compd.*, 2015, vol. 632, pp. 429–34.
22. X. Xu, L.Y. Chen, G.Q. Zhang, L.N. Wang, and J.Z. Jiang: *Intermetallics*, 2007, vol. 15, pp. 1066–70.
23. X.I.E. Zhiwei, Z. Yongzhang, Y. Yuanzheng, C. Xianzhao, T.A.O. Pingjun, Z. Xie, Y. Zhang, Y. Yang, X. Chen, and P. Tao: *Rare Met.*, 2010, vol. 29, pp. 444–50.
24. Y. Ke, F. Xinhui, L. Bing, L. Yanhong, and W. Xin: *Vacuum*, 2021, vol. 187, 110078.
25. K. Zhou, C. Chen, Y. Liu, S. Pang, N. Hua, W. Yang, and T. Zhang: *Intermetallics*, 2017, vol. 90, pp. 81–89.
26. K. Pajor, B. Rutkowski, Ł Gondek, P. Błyskun, M. Reehuis, K. Wiecek, and T. Kozieł: *Metall. Mater. Trans. A*, 2022, vol. 53A, pp. 2902–25.
27. M. Zinkevich: *Prog. Mater. Sci.*, 2007, vol. 52, pp. 597–647.
28. T. Kozieł, K. Pajor, and Ł Gondek: *J. Mater. Res. Technol.*, 2020, vol. 9, pp. 13502–08.
29. C.T. Liu, L. Heatherly, D.S. Easton, C.A. Carmichael, J.H. Schneibel, C.H. Chen, J.L. Wright, M.H. Yoo, J.A. Horton, and A. Inoue: *Metall. Mater. Trans. A*, 1998, vol. 29A, pp. 1811–20.
30. N.D.C. Neto, C. Soares, F.S. Pereira, V. Bergamaschi, S.G. Antonio, M.J. Kaufman, and M.F. de Oliveira: *J. Non. Cryst. Solids*, 2020, vol. 528, p. 119762.
31. Data retrieved from the Materials Project for Zr3Al2 (mp-13470) from database version 416 v2022.10.28.
32. Y. Xing, Y. Li, X. Wang, X. Yu, T. Zhang, and K. Georgarakis: *J. Non. Cryst. Solids*, 2016, vol. 452, pp. 30–34.
33. N.N. Greenwood and A. Earnshaw: *Chemistry of the Elements*, 2nd ed. Butterworth-Heinemann, Oxford, 1997.
34. Z. Altounian, E. Batalla, J.O. Strom-Olsen, and J.L. Walter: *J. Appl. Phys.*, 1987, vol. 61, pp. 149–55.
35. C.T. Liu, M.F. Chisholm, and M.K. Miller: *Intermetallics*, 2002, vol. 10, pp. 1105–112.
36. D. Wang, H. Tan, and Y. Li: *Acta Mater.*, 2005, vol. 53, pp. 2969–79.
37. C.P. Wang, S.B. Tu, Y. Yu, J.J. Han, and X.J. Liu: *Intermetallics*, 2012, vol. 31, pp. 1–8.
38. W. Zhou, Y. Meng, F. Duan, W. Huang, J. Yao, J. Pan, Y. Wang, and Y. Li: *Intermetallics*, 2021, vol. 129, pp. 1–6.
39. L. Yang, X.L. Wang, W.D. Porter, Z. Lu, A.D. Stoica, E.A. Payzant, J. Almer, and D. Shi: *Adv. Eng. Mater.*, 2008, vol. 10, pp. 1043–47.
40. Z. Long, W. Liu, M. Zhong, Y. Zhang, M. Zhao, G. Liao, and Z. Chen: *J. Therm. Anal. Calorim.*, 2018, vol. 132, pp. 1645–60.
41. R. Deng, Z. Long, L. Peng, D. Kuang, and B. Ren: *J. Non. Cryst. Solids*, 2020, vol. 533, 119829.

Publisher's Note Springer Nature remains neutral with regard to jurisdictional claims in published maps and institutional affiliations.